Improving the McClear model estimating the downwelling solar radiation at ground level in cloud-free conditions – McClear-v3

Benoît Gschwind, Lucien Wald, Philippe Blanc, Mireille Lefèvre, Marion Schroedter-Homscheidt, Antti Arola

Meteorol. Z. (Contrib. Atm. Sci.), Vol. **28**, No. 2, 147–163 (published online March 25, 2019)

Improving the McClear model estimating the downwelling solar radiation at ground level in cloud-free conditions – McClear-v3

Benoit Gschwind[1*], Lucien Wald[1], Philippe Blanc[1], Mireille Lefèvre[1], Marion Schroedter-Homscheidt[2] and Antti Arola[3]

[1]MINES ParisTech, PSL Research University, O.I.E. – Center for Observation, Impacts, Energy, Sophia Antipolis, France
[2]German Aerospace Center (DLR), Institute of Networked Energy Systems, Oldenburg, Germany
[3]Finnish Meteorological Institute, Kuopio, Finland

(Manuscript received September 27, 2018; in revised form February 7, 2019; accepted February 11, 2019)

Abstract

The fast McClear clear-sky model estimates the downwelling shortwave direct and diffuse irradiances received at ground level under cloud-free conditions. Several improvements are presented. They focus on the modeling of changes in irradiances with the solar zenithal angle and on a better exploitation of the aerosol properties offered by the Copernicus Atmosphere Monitoring Service (CAMS). Irradiances from this new version McClear-v3 were compared to 1 min measurements made in cloud-free conditions at 11 stations belonging to the Baseline Surface Radiation Network and being located in various climates. The correlation coefficient ranges between 0.982 and 0.999 for the global irradiance. The bias is positive (overestimation) and ranges between 1 W m^{-2} (0.1 % of the mean observed irradiance) and 20 W m^{-2} (3.2 %), with the exception of Barrow in Alaska (18 W m^{-2}). The standard deviation ranges between 16 W m^{-2} (2.3 %) and 30 W m^{-2} (3.8 %). The correlation coefficient for the direct irradiance ranges between 0.902 and 0.995. As expected, since the direct in McClear does not comprise any circumsolar contribution, the bias is negative (underestimation) and ranges between 49 W m^{-2} (7.7 %) and 5 W m^{-2} (0.7 %), with two exceptions: Sede Boqer (79 W m^{-2}) and Brasilia (13 W m^{-2}). The standard deviation is comprised between 34 W m^{-2} (5.3 %) and 69 W m^{-2} (10.7 %). These results are similar to those obtained with McClear version 2. Compared to the latter, McClear-v3 removes several artifacts and its estimates are continuous in space and time.

Keywords: solar radiation, clear-sky model, aerosol, CAMS, BSRN

1 Introduction

Solar radiation is the main driver behind the weather and climate systems on the planet. The downwelling solar irradiance received at ground level on horizontal surfaces and integrated over the whole spectrum is called here the surface solar irradiance, abbreviated as SSI. The SSI in cloud-free conditions depends on the composition of the atmosphere, including the aerosol properties and content in water vapor. A model estimating the SSI in cloud-free condition is called a clear-sky model and provides realistic upper limits of the SSI. Clear-sky models play a major role in methods for the assessment of the all-sky SSI from satellite images (see e.g. Cano et al., 1986; Deneke et al., 2008; Mueller et al., 2009; Posselt et al., 2012; Qu et al., 2017; Raschke et al., 1987; Rigollier et al., 2004).

McClear is such a clear-sky model. The original McClear model described in Lefèvre et al. (2013) was set into operation in 2012. It was slightly modified in 2013 yielding the version McClear-v2. Though it can be used as standalone model, McClear has mostly been used in synergy with the 3 h estimates of aerosol properties and daily total column contents of water vapor and ozone provided by the Copernicus Atmosphere Monitoring Service (CAMS) as inputs. The McClear service is the combination of McClear and CAMS (Schroedter-Homscheidt, 2018). It delivers time series of global, direct, diffuse and direct normal SSI at any site in the world and for any period comprised between 2004 and 2 days before today for the summarizations of 1 min, 15 min, 1 h, 1 day, and 1 month.

The outputs of the McClear service have been validated by comparisons with high quality measurements of the global, direct or diffuse SSI against ground-based measurements in different climates e.g. (Ceamanos et al., 2014a; Cros et al., 2013; Dev et al., 2017; Eissa et al., 2015a,b; Ineichen, 2016; Lefèvre et al., 2013; Lefèvre and Wald, 2016; Zhong and Kleissl, 2015). These authors reported very good results thus demonstrating the quality of the McClear service and indirectly the quality of the CAMS aerosol properties.

*Corresponding author: Benoit Gschwind, MINES ParisTech, PSL Research University, O.I.E. – Center for Observation, Impacts, Energy, B.P. 207 1, Rue Claude Daunesse, F-06904 Sophia Antipolis Cedex, France, e-mail: benoit.gschwind@mines-paristech.fr

The McClear service has several hundreds of users, made of academics, researchers, consultants and companies in various domains. They provide valuable validations of the McClear service and feedbacks on its limitations, from which we identified several issues in the model McClear-v2 itself.

This paper describes how we tackled several of these issues to yield McClear-v3. We assessed the benefits of the changes by comparing McClear-v3 to McClear-v2 and by comparing against ground measurements of SSI. Section 2 is an overview of McClear-v1 and McClear-v2. Section 3 lists the identified drawbacks; it describes the changes brought to overcome these issues and shows the improvements. Section 4 presents the measurements of the SSI performed in the BSRN network that serve as a reference to quantify the uncertainties of McClear-v2 and -v3. The measurements dataset is exactly the same as used by Lefèvre et al. (2013) for McClear-v1. The results of the comparison of the BSRN measurements with the outputs of McClear-v3 on the one hand and McClear-v2 on the other hand are given in Section 5. Section 6 concludes the paper and draw conclusions on the benefits of McClear-v3.

2 Overview of McClear-v1 and McClear-v2

Let D, B, and G denote respectively the diffuse, beam (also called direct), and global SSI:

$$G = D + B \tag{2.1}$$

Let E_{0N} denote the solar irradiance integrated over the whole spectrum impinging on a plane normal to the sun rays located at the top of the atmosphere at a given time. Let define the total solar irradiance, noted E_{TSI}, as the yearly average of E_{0N} during a year (Meftah et al., 2014). When the distance between the Earth and the Sun is equal to 1 astronomical unit, i.e. the eccentricity is equal to 1, then $E_{0N} = E_{\mathrm{TSI}}$.

Let E_0 denote the irradiance received on a horizontal plane located at the top of the atmosphere:

$$E_0 = E_{0N} \cos(\theta) \tag{2.2}$$

where θ is the solar zenithal angle. The clearness indices KT, KT_D and KT_B are obtained by dividing respectively G, D and B by E_0:

$$\begin{aligned} \mathrm{KT} &= G/E_0 \\ \mathrm{KT}_D &= D/E_0 \\ \mathrm{KT}_B &= B/E_0 \\ \mathrm{KT} &= \mathrm{KT}_D + \mathrm{KT}_B \end{aligned} \tag{2.3}$$

As described in Lefèvre et al. (2013), the McClear model aims at accurately estimating D, B, and G in cloud-free conditions. Actually, McClear-v1 computes firstly KT and KT_B, and derives G and B from this, D being known by Eq. (2.1).

The McClear-v1 model requires several inputs:

- the solar zenithal angle θ. In the McClear-v1 service, θ is computed with the SG2 algorithm (Blanc and Wald, 2012) knowing the geographical coordinates and the time;
- the three model parameters, called f_{iso}, f_{vol}, and f_{geo} (Schaaf et al., 2002) that describe the bidirectional reflectance distribution function of the ground. In the McClear-v1 service, these parameters are taken from the twelve monthly maps derived from the MODIS datasets proposed by Blanc et al. (2014b);
- the vertical profiles of temperature, pressure, density, and volume mixing ratio for gases as a function of altitude are taken from the USA Air Force Geophysics Laboratory (AFGL) standard atmosphere as implemented in libRadtran.
- the total column contents of ozone and water vapor. In the McClear-v1 service, these quantities are derived from CAMS;
- the aerosol optical depth (AOD) at 550 nm, the Ångström exponent, and one of the nine OPAC (Optical Properties of Aerosols and Clouds, Hess et al. 1998) aerosol mixtures: urban, continental clean, continental polluted, continental average, maritime clean, maritime polluted, maritime tropical, Antarctic, and desert, as implemented in libRadtran. In the McClear-v1 service, the AODs at 550 nm and 1240 nm are taken from CAMS, the Ångström exponent is computed from these two AODs, and the aerosol mixture is derived from the five partial AODs at 550 nm for dust, organic, sea salt, sulphate, and black carbon aerosol species from CAMS outputs using an empirical algorithm described in Lefèvre et al. (2013, see Fig. 1). The algorithm is a decision tree based on location, absolute optical depth, and relative optical depth. For instance the algorithm will select antarctic mixture for latitude greater than 70° or less than −60°. If it is not any antarctic mixture, it will select maritime clean or continental clean if the AOD is less than 0.05, and so on. This decision tree uses absolute thresholds of AOD which may cause a jumping from one mixture to the other while the AOD is changed only slightly, but is located close to a threshold.

The five vertical profiles of temperature, pressure, density, and volume mixing ratio for gases are: tropics (coded afglt), mid-latitude summer and winter (afglmls and afglmlw), and sub-Arctic summer and winter (afglss and afglsw). The McClear-v1 select one of those atmospheric profiles based on the location and the period of the year.

McClear-v1 uses abaci, also known as lookup tables, to solve the complex radiative transfer in the atmosphere. The computation of the abaci was made with the DISORT solver from the radiative transfer model libRadtran v1.7 (Mayer and Kylling, 2005). Each node of the abaci contains KT_B for a ground albedo equal to 0 and three values of KT, for ground albedo equal to 0, 0.1, and 0.9 respectively. The computation for any set of

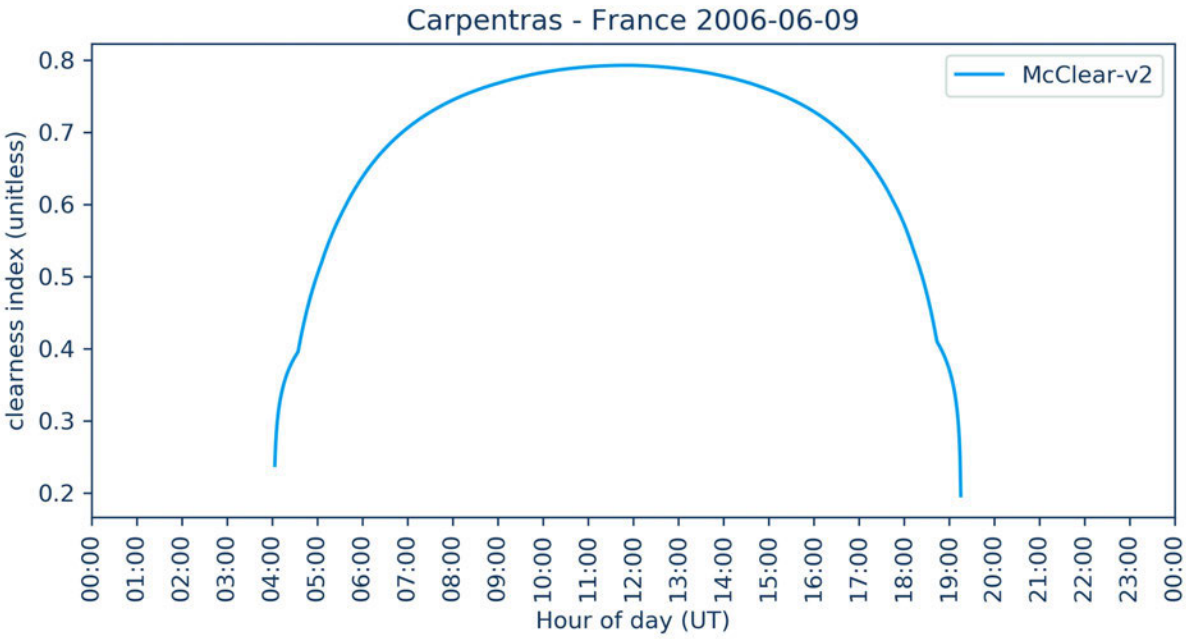

Figure 1: Daily profile of clearness index at Carpentras on 2006-06-09 for McClear-v2. Two abrupt changes are seen around 05:00 and 19:00 UT.

inputs is made by interpolating KT and KT_B. A full description of the abaci, the nodes and their selection, and interpolation functions may be found in Lefèvre et al. (2013).

The selection of the atmospheric profile in McClear-v1 produced spatial discontinuity. To solve this issue in McClear-v2 we use a map made of three layers covering the whole world established from a Köppen climate classification map (Peel et al., 2007). Each pixel of a layer bears a weight for each atmospheric profile: tropic, mid-latitude or sub-Arctic. It ranges from 0.0 to 1.0. If the value 1.0 for a given profile it means that this pixel belongs to this class of profile and that there is no chance that it may belong to another. On the contrary, if it is 0.0, then there is no chance that this pixel belongs to this profile. For each pixel the sum of the weights in the three layers is equal to 1.0. In operations, at a given pixel, the SSI is computed for each of the three profiles, yielding $(G1, B1)$, $(G2, B2)$ and $(G3, B3)$. The SSI G and B are the weighted averages of the three values using the weights of the layer. This was the unique change between McClear-v1 and -v2, this change does not change the result for most locations.

3 Identified drawbacks and proposed changes from McClear-v2 to McClear-v3

3.1 Better handling the summer-winter transition

In McClear-v2 the transition in atmospheric profile from winter to summer and reciprocally is abrupt. The boreal summer is defined from 1 April to 31 October both included, and the boreal winter covers the remaining months. This switch is noticeable in long time series because it always occurs at the same calendar date. This may impede analysis of long term averages or analysis of variability of time series. To avoid this abrupt change, we adopted a weighted average based on the solar declination δ to ensure a smooth transition, as follows:

$$\begin{aligned} B(t) = {} & Bs(t)[(\delta_{\max} + \delta(t))/(2\delta_{\max})] \\ & + Bw(t)[(\delta_{\max} - \delta(t))/(2\delta_{\max})] \\ D(t) = {} & Ds(t)[(\delta_{\max} + \delta(t))/(2\delta_{\max})] \\ & + Dw(t)[(\delta_{\max} - \delta(t))/(2\delta_{\max})] \end{aligned} \tag{3.1}$$

where t is the time, $\delta_{\max}$ is the maximum solar declination, about 23.4°. Bs and Ds are the direct and diffuse SSI obtained when running the McClear model for the whole year with the summer profile; Bw and Dw are the direct and diffuse SSI obtained when running the McClear model for the whole year with the winter profile. δ is currently computed with the SG2 algorithm (Blanc and Wald, 2012). Declination is a suitable approach as it is related to the diurnal duration which varies between summer and winter systematically. This is taken as a proxy to merge the typical climatological patterns being described by summer and winter atmospheres as described in standard atmospheres. In this way, the issue of the discontinuity in time is satisfactorily solved at the expenses of two runs of McClear instead of one.

3.2 A new function for interpolating the SSI from the solar zenithal angle

Another discontinuity originates from the interpolation function of KT and KT_B with θ. Lefèvre et al. (2013) adopted the modified Beer-Lambert (MLB) function proposed by Mueller et al. (2004) with five segments: $[0, 60]°$, $[60, 75]°$, $[75, 80]°$, $[80, 85]°$ and $[85, 89.9]°$ to reduce the number of nodes in abaci and save computer memory. Separate interpolations are performed in each segment with continuity of KT and KT_B at each limit. However, their derivatives are not continuous and this creates abrupt changes at interval boundaries. In addition, though the amplitudes of the errors are small, they are the greatest for large θ (Qu et al., 2011). These discontinuities occur at the beginning and end of the day when $\theta > 60°$ and were also reported by Ineichen (2016). The MLB interpolation also does not capture well the changes in clearness indices and SSI at large θ, and it does not provide results for $\theta \geq 90°$ because of its definition. This is an issue for an accurate assessment of the diffuse SSI.

Fig. 1 shows this issue in a time series of KT given by McClear-v2 at Carpentras, in France, on 2006-06-09. One can see abrupt changes of the slope of the curve in the blue curve at 05:00 UT and 19:00 UT.

We looked for a new function with a limited number of parameters that does not exhibit such discontinuities and offers a better accuracy than the MLB. In the process, about 50 either physically or numerically motivated fit functions were created by using different interpolation techniques: piecewise linear interpolation, polynomial fitting, and barycentric interpolant. Interpolations of G, B, and D and several other related quantities such as KT, $\log(G)$, etc. were tested. Furthermore, several interpolation variables linked to θ such as θ itself, $\cos(\theta)$, $\arccos(\theta)$, $\log(1 + \cos(\theta))$, or outputs of various airmass functions were evaluated.

Performances of each function were assessed by comparing its outputs against a reference dataset of SSI. We created the latter from several runs of the DISORT solver from libRadtran to produce a set of 1000 representative atmospheric conditions. For this purpose, a Monte-Carlo technique was used to select the 6 inputs to libRadtran representing the atmospheric conditions: total column content of ozone and water vapor, aerosol optical thickness and mixture, atmospheric profile, and elevation of the ground above mean sea level. The selection took into account the modeled marginal distribution established from observations by Oumbe et al. (2014). Table 1 reports the range of values of each variable and the model for marginal probability. The distance between the sun and the Earth was set to 1 astronomical unit, the ground albedo was set to 0.2. For each atmospheric condition, we computed the SSI for θ between 0° and 90° by step of 0.1°.

We computed the differences between the reference dataset and the results of a given function, and then their mean and standard deviation. Furthermore, we created bins of θ and for each bin, we computed the mean, the minimum, and the maximum of the differences. The Figs. 2, 3 and 4 are plots of these values for several functions.

Fig. 2 is the plot for G given by the 5-piecewise MLB interpolation. One may see that the amplitude of errors is large for $\theta < 60°$, the minimum is less than $-2\,\mathrm{W\,m^{-2}}$ and the maximum is greater than $3\,\mathrm{W\,m^{-2}}$. As θ increases, the error tends to be positive yielding an overestimation of G. We observe bounces at 60°, 75°, 80°, 85° and 89.9° which induce strong changes in slope at these nodes. Such changes in slope are visible in daily profiles of SSI and clearness indices as already illustrated in Fig. 1.

The same piecewise MLB function but with a greater number of nodes were tested. Fig. 3 is the result for G using 9 nodes. The estimates are more accurate than with the 5-piecewise MLB function but still exhibit large changes of slope for θ around 90°.

Fig. 4 is the result of the piecewise linear interpolation using 19 nodes, i.e. θ ranging from 0° to 90° by step of 5°. We observe a discontinuity in derivative at each node and that the errors are large for the greatest θ.

We scrutinized all plots, biases and standard deviations to select a function to find a tradeoff between the smallest errors and the smallest number of parameters needed for a given function to limit the size of abaci. Our choice was the following function that applies to the normalized quantities B^* and D^* which are equal to B and D normalized by E_{0N}:

$$B^* = B/E_{0N} = KT_B cos(\theta) \qquad (3.2)$$
$$D^* = D/E_{0N} = KT_D cos(\theta)$$

It was found that a polynomial of degree 8, which need 9 parameters, in $\log(1+\cos(\theta))$ can be accurately fit onto the series of B^* and D^* for each of the 1000 cases:

$$B(\theta) = \sum_{n=0}^{8} a_n [\log(1 + \cos(\theta))]^n \qquad (3.3)$$

Unexpectedly, it happens that the same function was the best choice for D^*. The usual approach to compute a_n consists in fitting the polynomial function with a set of pairs (x, y) where x is the input to the function and y its result. This requires generating a large number of pairs; in our case this requires a large amount of computer resources because the pairs must be generated by the DISORT solver, but, if you can compute any pair (x, y), it is possible to generate only $N + 1$ (x, y) pairs to fit a polynomial function of degree N using Chebyshev nodes. By the means of Chebyshev polynomials of the first kind, we obtain the nine Chebyshev nodes, i.e. the values of $\log(1 + \cos(\theta))$ that are optimal for the computation of a_n over the range $[0, 90]°$, with respect to the maximum absolute error within this range. These nodes yield nine equivalent nodes in θ which are: 8.31°, 24.59°, 39.90°, 53.68°, 65.53°, 75.15°, 82.42°, 87.27°, and 89.69°.

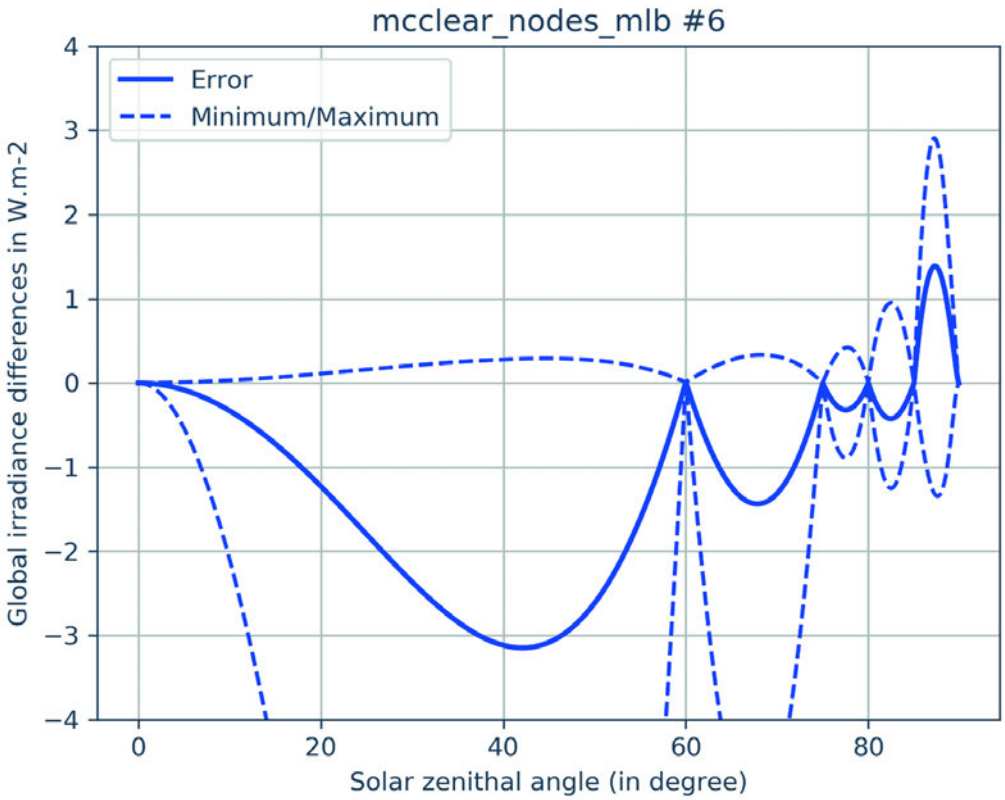

Figure 2: Differences between the results of the 5-piecewise MLB interpolation used in McClear-v2 and DISORT solver from libRadtran outputs for the global irradiance. The full line is the average of the errors for the 1000 cases and the dashed lines are the minimum and the maximum of the errors.

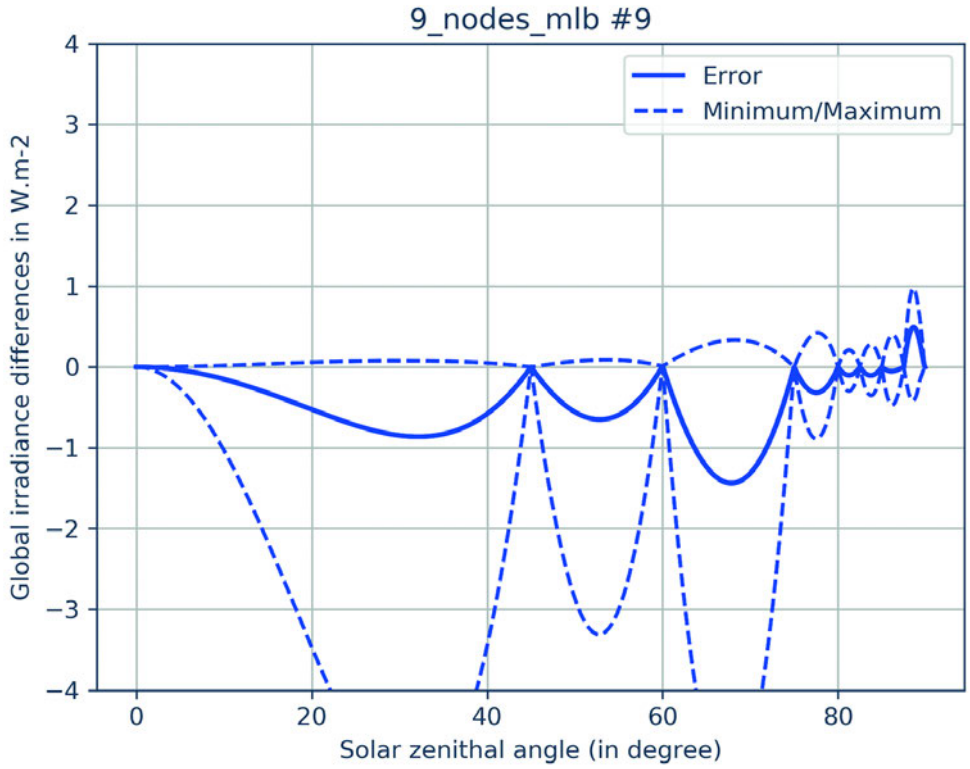

Figure 3: Differences between the results of a 8-piecewise MLB interpolation and libRadtran outputs for the global irradiance. The full line is the average of the errors for the 1000 cases and the dashed lines are the minimum and the maximum of the errors.

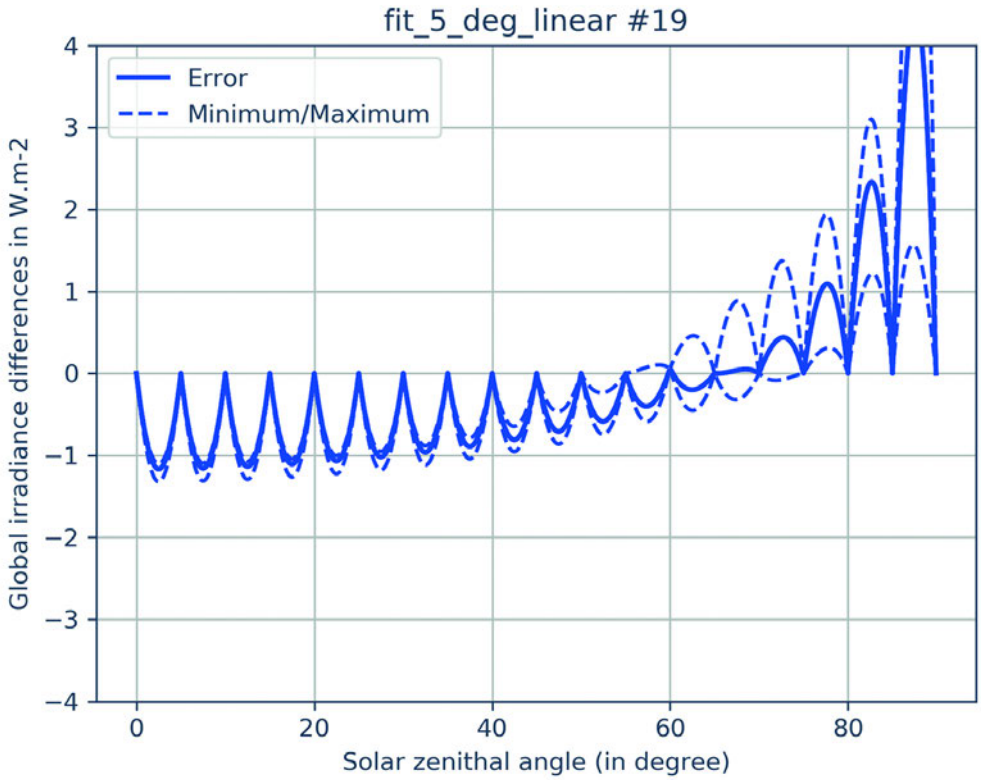

Figure 4: Differences between the results of the linear interpolation every 5° and libRadtran outputs for the global irradiance. The full line is the average of the errors for the 1000 cases and the dashed lines are the minimum and the maximum of the errors.

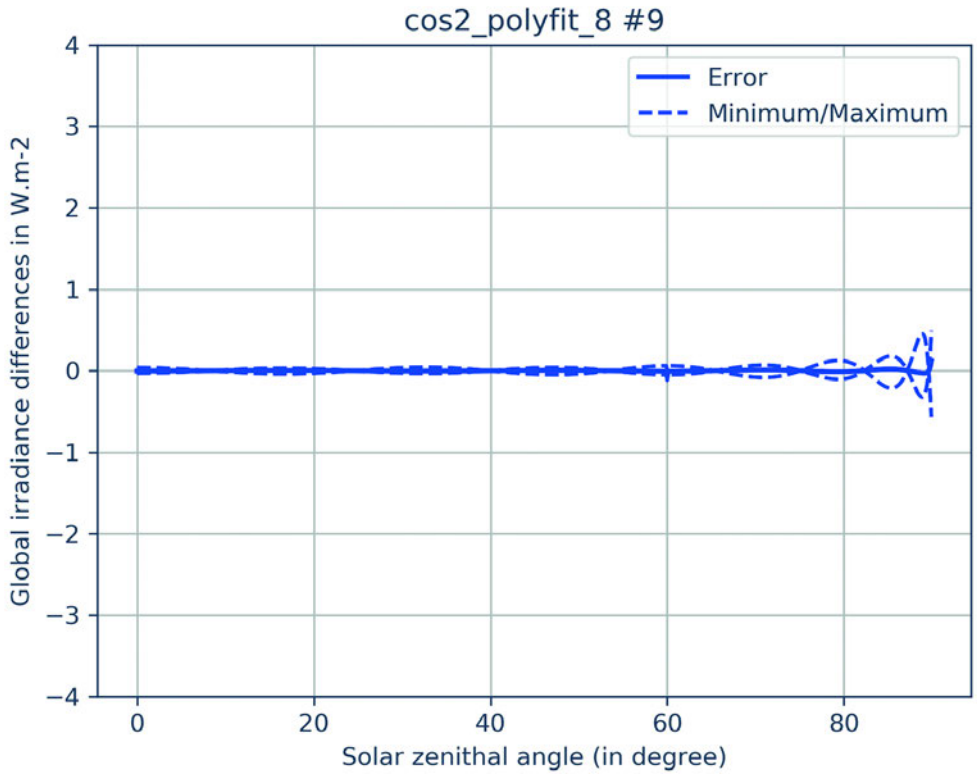

Figure 5: Differences between the results of the selected function and outputs of DISORT solver from libRadtran for the global irradiance. The full line is the average of the errors for the 1000 cases and the dashed lines are the minimum and the maximum of the errors.

Table 1: Range of values for 6 variables describing the cloud-free atmosphere. After Oumbe et al. (2014, their Table 4).

Variable	Range of values and model for marginal probability
Total column content in ozone	Ozone content is $300 * \beta + 200$, in Dobson unit where β follows a Beta law, with parameters $A = 2$, and $B = 2$
Total column content in water vapor	Equiprobable between 0 and 70, in kg m^{-2}
AOD at 550 nm	Gamma law, with shape parameter = 2, and scale parameter = 0.13
Aerosol mixture	Equiprobable in the set of the nine OPAC aerosol mixtures
Atmospheric profile	Equiprobable in the set: mid-latitude summer, mid-latitude winter, sub-Arctic summer, sub-Arctic winter, tropical
Elevation of the ground above mean sea level	Equiprobable in the set: 0, 1, 2, 3 in km

For each of the 1000 cases, B^* and D^* at each of these nine nodes, and then B and D were computed. Fig. 5 exhibits the mean, maximum and minimum of the differences between the reference datasets and the results of the selected function for G. One may see that the errors are very small, i.e. less than 0.7 W m^{-2}, for any θ. There are no discontinuities in the first derivatives. Similar results are attained for B and D. The case of $\theta > 90°$ has not been treated. However, the present approach may be extended to such cases provided libRadtran is run with an appropriate solver such as MYSTIC (Emde et al., 2016).

3.3 Better exploiting the CAMS aerosol properties

The CAMS service provides several aerosol properties including the total AOD at 550 nm, τ_{550}, and other wavelengths, and partial AODs at 550 nm for sea salt (SS, τ_{550-SS}), dust (DU, τ_{550-DU}), organic matter (OM, τ_{550-OM}), black carbon (BC, τ_{550-BC}), and sulfates (SU, τ_{550-SU}) aerosol species. These five partial optical depths are inputs into an empirical algorithm (Lefèvre et al., 2013) to yield one of the nine OPAC aerosol mixtures adopted in McClear-v2. The use of this classification creates discontinuities in time series of SSI as well as in maps because the algorithm can switch from one mixture to another without any transition. This is illustrated in Fig. 6 which exhibits the daily profile of G at Carpentras on 2006-06-10 and is one case of failure reported by Lefèvre et al. (2013). Here, the aerosol mixture was classified as "urban" during the day at the BSRN station Carpentras (France). From 08:00 to 11:30 UT, the mixture was erroneously classified as "maritime polluted", yielding a 3 % increase in G.

The issue was fixed by replacing the classification by a smoother approach proposed by Ceamanos et al. (2014b). It consists in firstly computing a partial SSI for each aerosol component and then computing the SSI for the actual atmosphere by mixing the partial SSIs. Implementing their approach was not straightforward because the CAMS outputs have to be mapped onto the libRadtran inputs.

The database OPAC in libRadtran comprises among others, microphysical and optical properties of 10 aerosol components:

- INSO: insoluble (soil particles with a certain amount of organic material),
- WASO: water-soluble (sulfates, nitrates & other water-soluble substances),
- SOOT: soot (absorbing black carbon),
- SSAM: sea salt accumulation mode (various kinds of sea salt contained in seawater),
- SSCM: sea salt coarse mode (various kinds of salt contained in seawater),
- MINM: mineral nucleation mode (a mixture of quartz and clay minerals),
- MICM: mineral coarse mode (a mixture of quartz and clay minerals),
- MIAM: mineral accumulation mode (a mixture of quartz and clay minerals),
- MITR: mineral-transported (desert dust transported over long distances with a reduced amount of large particles),
- SUSO: sulfate droplets (75 % solution of H_2SO_4, for stratospheric aerosols).

Morcrette et al. (2009) mentioned that optical properties of aerosols in CAMS are taken from the OPAC aerosol components. The CAMS organic matter OM is distributed between 50 % of hydrophilic matter which are assigned here to the OPAC WASO component, and 50 % of hydrophobic matter that are assigned to the OPAC INSO component. For black carbon BC, 80 % are considered as hydrophobic and are assigned to the SOOT component, and 20 % are considered as hydrophilic and are assigned to the WASO component. The sulfates SU are assigned to the WASO component. As for the naturally originated aerosols, the CAMS sea salt SS is assigned to the sum of the OPAC SSAM and SSCM components, and the CAMS dust DU is assigned to the sum of the OPAC mineral components: MINM, MICM and MIAM, similarly to Ceamanos et al. (2014b). In the following, for the sake of the simplicity, the sum of the SSAM and SSCM components is denoted as the SALT component, and the sum of the MINM, MICM and MIAM components is denoted as the DUST component.

If τ_{550-X} denotes the optical depth at 550 nm for the component X, the optical depths for the five components INSO, WASO, SOOT, SALT and DUST, may be deduced from the CAMS aerosol species using the

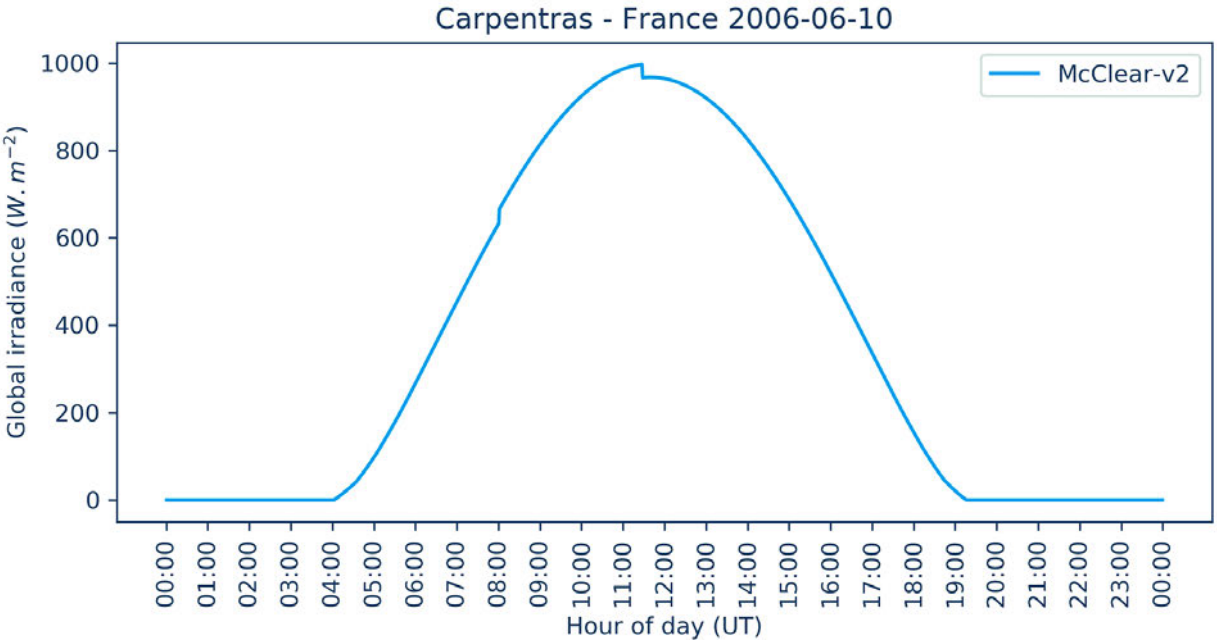

Figure 6: Daily profile of the global irradiance at Carpentras on 2006-06-10 for McClear-v2. It exhibits abrupt changes around 08:00 and 11:30 UT.

above-listed assignations, according to Ceamanos et al. (2014a) appendix B1, which is itself following Morcrette et al. (2009):

$$\begin{aligned}
\tau_{550\text{–INSO}} &= 0.5\tau_{550\text{–OM}} \\
\tau_{550\text{–WASO}} &= \tau_{550\text{–SU}} + 0.5\tau_{550\text{–OM}} + 0.2\tau_{550\text{–BC}} \\
\tau_{550\text{–SOOT}} &= 0.8\tau_{550\text{–BC}} \\
\tau_{550\text{–SALT}} &= \tau_{550\text{–SSAM}} + \tau_{550\text{–SSCM}} = \tau_{550\text{–SS}} \\
\tau_{550\text{–DUST}} &= \tau_{550\text{–MINM}} + \tau_{550\text{–MICM}} + \tau_{550\text{–MIAM}} \\
&= \tau_{550\text{–DU}}
\end{aligned} \tag{3.4}$$

This mapping assumes that the distribution between hydrophilic and hydrophobic matter remains constant over the time. This hypothesis does not take into account the change in this distribution due to the absorption of water in the atmosphere and the different lifetimes of aerosols.

Regarding the vertical distribution, an empirical approach was adopted here wherein the vertical distribution for each of the five CAMS components is a modified version of a distribution of one of the nine aerosol mixtures as defined by OPAC:

- INSO: "continental average" vertical distribution where all components but INSO were set to 0.0;
- WASO: "continental average" vertical distribution where all components but WASO were set to 0.0;
- SOOT: "urban" vertical distribution where all components but SOOT were set to 0.0;
- SALT: "maritime clean" vertical distribution where WASO, INSO, SOOT, MINM, MICM and MIAM were set to 0.0;
- DUST: "desert" vertical distribution where WASO, INSO, SOOT, SSAM and SSCM were set to 0.0.

Following Ceamanos et al., (2014b), the partial clearness indices KT_X and KT_{B-X} of the cloud-free atmosphere are computed for each of the five components separately but using the total aerosol optical depth τ_{550}. Then, the actual clearness indices KT and KT_B are computed by a weighted average of KT_X and KT_{B-X} using partial aerosol optical depths: $\tau_{550\text{–INSO}}$, $\tau_{550\text{–WASO}}$, $\tau_{550\text{–SOOT}}$, $\tau_{550\text{–SALT}}$, and $\tau_{550\text{–DUST}}$:

$$KT = \sum \frac{\tau_{550X} * KT_X(\tau_{550})}{\tau_{550}} \tag{3.5}$$

A similar equation holds for KT_B. This approach does not create discontinuities. This is illustrated in Fig. 7 where the daily profile of G estimated with McClear-v3 does not exhibit any of the discontinuities found in the daily profile from McClear-v2. One may conclude that this approach is satisfactory at the expense of more runs of the McClear model, one for each component.

3.4 Reshaping the abaci

The abaci must be reshaped in order to account for the proposed changes discussed above. Years of exploitation of McClear-v2 did not indicate any flaw in the selection of the nodes of the abaci. Thus we kept the same nodes except for θ, and for aerosol properties. The list of nodes for each of the entries of the abaci of McClear-v3 is:

- total column content in ozone (in Dobson unit): 200, 300, 400, 500,
- total column content in water vapor (kg m^{-2}): 0.1, 3, 5, 7, 10, 15, 20, 30, 40, 60, 80, and 100,
- τ_{550}: 0.01, 0.05, 0.1, 0.2, 0.3, 0.5, 1, 1.5, 2, and 5,
- aerosol component: WASO, INSO, SOOT, SALT, DUST,

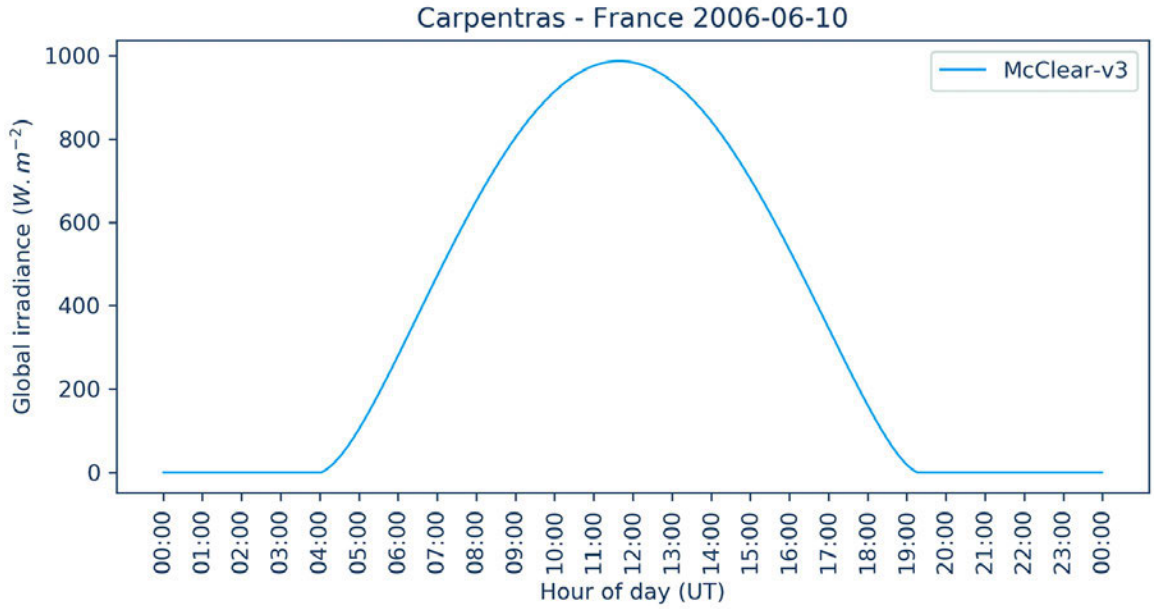

Figure 7: Daily profile of the global irradiance at Carpentras on 2006-06-10 for McClear-v3. It does not exhibits abrupt changes around 08:00 and 11:30 UT.

- vertical profiles of temperature, pressure, density, and volume mixing ratio for gases: tropics (afglt), mid-latitude summer and winter (afglmls and afglmlw), and sub-Arctic summer and winter (afglss and afglsw).
- site elevation above mean sea level (km): 0, 1, 2, 3, 4, 5, 6, and 7,
- elevation above ground level (km): 0, 0.5, 1, 1.5, and 2.

The abacus of McClear-v3 has about $15 \cdot 10^6$ nodes, which is 10 times less than the abaci of McClear-v2, this is mostly due to the removing of the Ångström exponent, which was not needed anymore, and reduction of aerosol mixture from 9 down to 5. Note that the solar zenithal angle θ is not one of the direct entries of abaci that gives the nine corresponding coefficients of the interpolation functions with respect θ. The abacus is computed for the distance between the Earth and the Sun equal to 1 astronomical unit, i.e. $E_{0N} = E_{\mathrm{TSI}}$; a correction depending on the Sun-Earth distance is be applied afterwards. Whereas a node in McClear-v2 bears KT_B for a ground albedo equal to 0 and three values of KT, for ground albedo equal to 0, 0.1, and 0.9 respectively, a node in McClear-v3 bears more data as it bears several sets of the nine coefficients of the selected function for θ, namely to compute B^* for a ground albedo equal to 0, and to compute values of D^* for ground albedo equal to 0, equal to 0.1, and equal to 0.9,

Operations of McClear-v3 are similar to those of McClear-v2 described in Lefèvre et al. (2013) with the exceptions that computations, interpolations between nodes and estimates at any θ are performed with B^* and D^* instead of KT and KT_B. It was checked that there is no influence of the order of applications of the n-linear interpolations and polynomial in θ.

3.5 Changing the total solar irradiance

The value recommended for the total solar irradiance E_{TSI} has varied over the recent decades as the instrumentation was more and more accurate. The value adopted for E_{TSI} in McClear-v2 was 1367 W m^{-2}. Recent measurements of E_{TSI} in 2010 yield 1362 W m^{-2} with an uncertainty of order of 2 W m^{-2} (Meftah et al., 2014), in agreement with the International Astronomical Union (2015). Thus we adopted this value of 1362 W m^{-2} in McClear-v3.

The sun is an active star and its activity includes changes in the intensity of solar radiation and ejection of solar material and by its appearance. The solar activity exhibits a nearly periodic 11-year cycle, each cycle being characterized by the number and size of sunspots, flares, and other manifestations. The solar cycle has a limited influence on the total solar irradiance, of order of 0.1 %. In other words, average changes during a cycle are small and of order of 1 W m^{-2}. Day-to-day changes in E_{0N} are greater and may reach 5 W m^{-2}, i.e. approximately 0.4 % of the total solar irradiance (Kopp and Lean, 2011).

4 The BSRN dataset and the protocol for validation

After having shown the improvements brought by McClear-v3 regarding several artifacts identified in McClear-v2, this section is dedicated to the validation of McClear-v3 against measurements of SSI performed at ground stations. We used the same reference dataset

Table 2: List of BSRN stations, their country, their geographical coordinates, and the period of measurements. Amsl: above mean sea level.

Station name	Country	Latitude (°)	Longitude (°)	Elevation amsl (m)	Period of measurements
Barrow	USA (Alaska)	71.323	−156.607	8	2005–2008
Palaiseau	France	48.713	2.208	156	2005–2007
Payerne	Swizerland	46.815	6.944	491	2005–2008
Carpentras	France	44.083	5.059	100	2005–2008
Xianghe	China	39.754	116.962	32	2005–2007
Tateno	Japan	36.050	140.133	25	2005–2008
Sede Boqer	Israel	30.905	34.782	500	2005–2008
Tamanrasset	Algeria	22.780	5.510	1385	2005–2008
Brasilia	Brazil	−15.601	−47.7130	1023	2006–2007
Alice Springs	Australia	−23,798	133.888	547	2005–2008
Lauder	New Zealand	−45.045	169.689	350	2005–2007

Table 3: List of climates and corresponding stations, according to Peel et al. (2007).

Climate	Stations
ET: polar climate in tundra	Barrow
Cfb: Temperate climate without dry season and warm summer	Palaiseau, Lauder
Dfb: Cold climate without dry season and warm summer	Payerne
Csb: Temperate climate with dry and warm summer	Carpentras
Dwa: Cold climate with dry winter and hot summer	Xianghe
Cfa: Temperate climate without dry season and hot summer	Tateno
BWh: Arid and hot climate of desert type	Sede Boqer, Alice Springs
BWh + mountain climate	Tamanrasset
AW: Tropical climate in savannah	Brasilia

as Lefèvre et al. (2013) which contains 1 min measurements of G and B in cloud free conditions collected at 11 stations of the Baseline Surface Radiation Network (BSRN, Table 2). These stations experience various climates as shown in Table 3.

Table 4 reports the number of measurements in cloud-free conditions and the means of G, B, KT, and KT_B.

The validation was made by comparing G and B of the reference dataset and the McClear-v3 estimates for coincident instants and location. The discrepancies at each instant were computed by subtracting the observations from the McClear-v3 estimates and they were summarized by the bias, the standard deviation, and the root mean square error. Relative values were expressed with respect to the means given in Table 4. The Pearson correlation coefficients, slopes and offsets of the least-squares fitting lines were also computed.

This comparison was performed for G, B, KT, and KT_B at each site, and all instants from all years. Additionally, results were evaluated for different years, different classes of θ, different classes of readings from CAMS: τ_{550}, total column contents in water vapor and ozone, and typical monthly Linke turbidity factors read from Remund et al. (2003).

The World Meteorological Organization (WMO, 2012) sets recommendations for achieving a given accuracy in measuring solar radiation. This document clearly states that "good quality measurements are difficult to achieve in practice, and for routine operations, they can be achieved only with modern equipment and redundant measurements." In this document, the typical relative uncertainty (95 % probability) of measurements of good quality is approximately 8 % for G and 2 % for B. The uncertainty targets are more stringent for BSRN measurements: 2 % for G and D and 0.5 % for B (Ohmura et al., 1998). Vuilleumier et al. (2014) performed a very detailed analysis on the uncertainty at the BSRN station of Payerne. They reported that the target can be achieved for G and D but not for B for which the uncertainty is approximately 1.5 %.

Like most of the radiative transfer models, libRadtran computes B without taking into account the circumsolar radiation which is then taken into account in D. On the opposite, the pyrheliometers like those in the BSRN network capture part of the circumsolar radiation with a half-angle aperture of about 2.5° (Blanc et al., 2014a). Hence, one may expect McClear-v3 to underestimate B measured at the BSRN sites because no correction is brought for the contribution due to the circumsolar area. As a consequence, one may expect McClear-v3 to overestimate D measured at the BSRN sites. The results hereafter will be presented for G and B, the former combining the over- and underestimation of its direct and diffuse components.

The pyranometers and pyrheliometers measure the solar radiation in the range [285, 2800] nm approximately while McClear provides the SSI for the range [240, 4606] nm. The difference in G and B in cloud-free conditions amounts to a few W m^{-2}. For the sake of this validation, a set of abaci was computed that fits the spectral range of the measurements. Similarly, we computed

Table 4: For each station, number of measurements in cloud-free conditions, means of global and direct SSI, and of clearness indices in cloud-free conditions.

Station	Number of measurements in cloud-free conditions	Mean 1 min irradiance ($W\,m^{-2}$) G	B	Mean 1 min clearness index KT	KT_B
Barrow	70283	498	406	0.760	0.616
Palaiseau	29222	598	492	0.719	0.586
Payerne	136879	629	530	0.731	0.612
Carpentras	300468	596	505	0.721	0.606
Xianghe	40644	791	642	0.749	0.608
Tateno	133433	590	485	0.727	0.598
Sede Boqer	304550	785	667	0.755	0.643
Tamanrasset	331045	791	653	0.797	0.663
Brasilia	73563	649	560	0.742	0.637
Alice Springs	442315	715	634	0.769	0.678
Lauder	117090	600	544	0.747	0.668

BSRN-specific abaci for McClear-v2 for comparing v2 and v3 against the BSRN measurements.

A limitation of the validation is the lack of large θ in the dataset from Lefèvre et al. (2013). Because of their criteria for selecting cloud-free instants, all instants are within [sunrise + 90 min, sunset − 90 min]. Hence, the improvements in interpolating the SSI as a function of θ angle will not be fully evidenced here.

5 Validation of McClear-v3 with BSRN data and comparison with McClear-v2

5.1 Global irradiance

Fig. 8 and Fig. 9 are examples of 2D histograms, also called scatter density plots, between the BSRN observations and the McClear-v3 estimates of G at Payerne and Xianghe selected for the sake of the comparison with the graphs in Lefèvre et al. (2013). Overall, a very good fit is observed between estimates and observations: the points are well aligned along the 1:1 line with a limited scattering, denoting a quasi-unbiased estimation of G.

Table 5 reports the correlation coefficient at each site as well as the slope of the fitting line for G. A perfect model will exhibit a correlation coefficient equal to 1.0, a slope equal to 1.0 and an offset equal to 0.0; the closer the values to these targets, the better. The correlation coefficients for McClear-v3 are very large and greater than 0.98 at all sites. Xianghe exibits the worst correlation coefficient. This is likely explained by the fact that Xianghe has a high black carbon optical depth strongly varying between 0 and 0.15 with an average of about 0.04 and the known difficulties in modeling both high and variable aerosol loads properly in the temporal resolution of 1 min used in our assessment. The slopes are comprised between 0.97 and 1.03, excepted at Barrow (0.94), Sede Boqer (0.96) and Tamanrasset (0.94). Table 5 reports also the correlation coefficients and slopes for McClear-v2. Though the values are very similar, slight improvements may be noted for v3; the correlation coefficients for v3 are greater than those for v2, and the slopes for v3 are slightly closer to 1.

Table 5: Results for global irradiance of the comparison of McClear-v3 versus BSRN side-by-side with those of the comparison of McClear-v2 versus BSRN. Correlation coefficient and slope of the line adjusted by least-squares fitting.

Station	Correl. coeff v2	Correl. coeff v3	Slope v2	Slope v3
Barrow	0.9940	0.9954	0.941	0.942
Palaiseau	0.9969	0.9983	1.001	1.023
Payerne	0.9970	0.9982	0.996	1.011
Carpentras	0.9978	0.9987	1.012	1.027
Xianghe	0.9735	0.9817	0.955	0.969
Tateno	0.9941	0.9971	0.991	1.020
Sede Boqer	0.9954	0.9974	0.934	0.960
Tamanrasset	0.9979	0.9978	0.944	0.941
Brasilia	0.9976	0.9977	1.013	1.017
Alice Springs	0.9989	0.9990	1.016	1.015
Lauder	0.9985	0.9988	1.011	1.009

The bias of McClear-v3 shown in Table 6 is positive, except at Barrow where the bias is $-18\,W\,m^{-2}$, i.e. −4 % in relative value. It ranges from 1 to $20\,W\,m^{-2}$, i.e. from 0 to 3 % in relative value. The greatest biases in absolute value are observed at Payerne, then Barrow and Carpentras; they are respectively equal to 20, 18 and $18\,W\,m^{-2}$. The standard deviation is fairly constant; it offers a limited range of variation between 16 and $24\,W\,m^{-2}$ except at Xianghe where it reaches $30\,W\,m^{-2}$. Relative standard deviations are small and range between 2 and 4 %.

As reported by Lefevre et al. (2013), one should note that the statistical quantities slightly vary from one year to another. For example, the bias at Alice Springs is 6, 4, 10 and $11\,W\,m^{-2}$ respectively in 2005, 2006, 2007, and 2008. Also noted by Lefevre et al. (2013), these statistical quantities vary with other variables: year, θ, τ_{550}, total column contents in water vapor and ozone, and typical monthly Linke turbidity factors but no clear

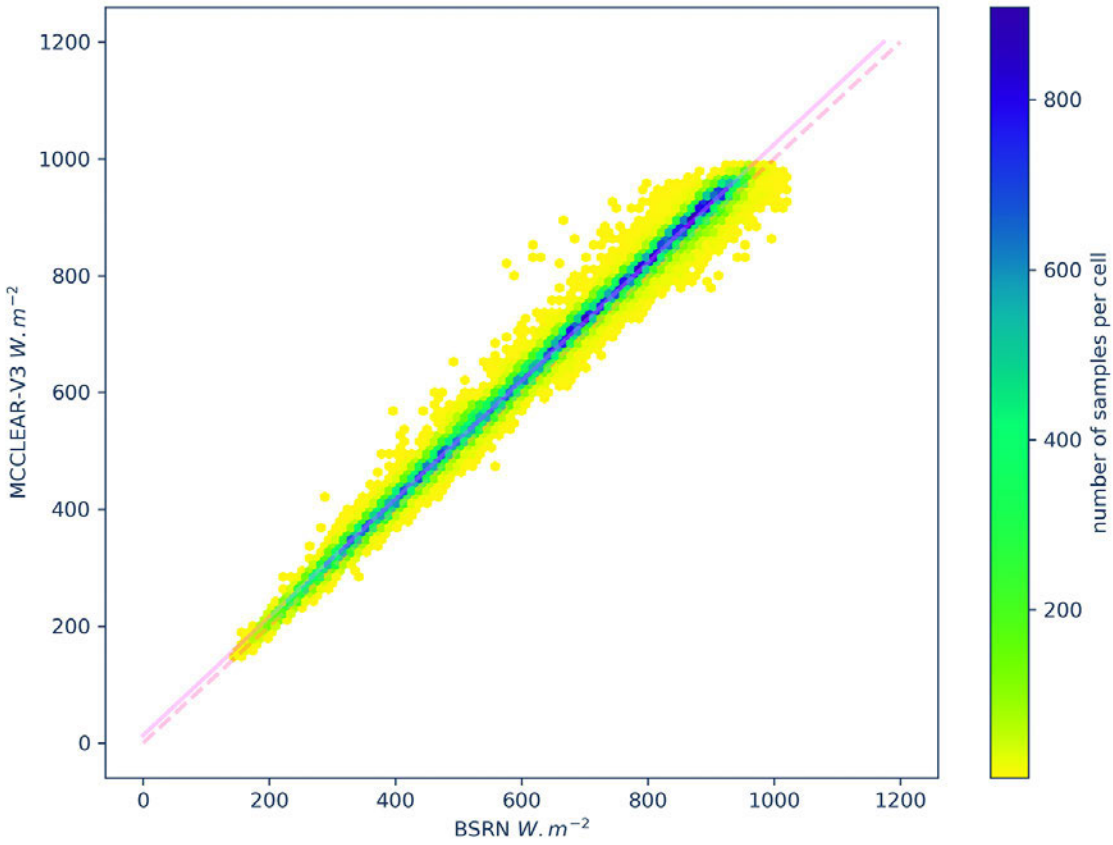

Figure 8: 2D histogram between BSRN observations (horizontal axis) and McClear-v3 estimates (vertical axis) for global irradiance at Payerne. The color indicates the number of pairs in each class. The pink dotted line is the identity line, the full line results from a least-square fitting.

Table 6: Results for global irradiance of the comparison of McClear-v3 versus BSRN side-by-side with those of the comparison of McClear-v2 versus BSRN. Bias and standard deviation and their values relative to the means of the measurements.

Station	Bias ($W\,m^{-2}$)		Standard deviation ($W\,m^{-2}$)		Relative bias (in %)		Relative standard deviation (in %)	
	v2	v3	v2	v3	v2	v3	v2	v3
Barrow	−16	−18	24	21	−3.2	−3.6	4.8	4.2
Palaiseau	1	7	23	18	0.1	1.1	3.9	3.1
Payerne	17	20	22	18	2.7	3.2	3.5	2.8
Carpentras	16	18	20	17	2.7	3.1	3.4	2.8
Xianghe	−11	8	36	30	−1.4	1.0	4.6	3.8
Tateno	13	10	28	21	2.2	1.7	4.8	3.5
Sede Boqer	7	13	28	21	0.9	1.6	3.6	2.7
Tamanrasset	9	1	23	24	1.1	0.1	2.9	3.0
Brasilia	17	16	22	21	2.6	2.5	3.4	3.3
Alice Springs	12	8	17	16	1.7	1.0	2.4	2.3
Lauder	10	6	19	18	1.6	1.0	3.2	2.9

trend can be seen. Given the great correlation coefficients, the proximity to 1 of the slopes and the small standard deviations of errors, one may conclude that McClear-v3 is capable of accurately capturing the variability of G at 1 min time-scale.

Table 6 reports also the bias and standard deviation for v2. They are similar to those for v3. One notes an improvement in standard deviation from v2 to v3. It ranges from 17 to 36 $W\,m^{-2}$ for v2 and is less for v3 with a range $[16, 30]\,W\,m^{-2}$.

5.2 Beam irradiance

Fig. 10 and Fig. 11 are examples of 2D histograms between the BSRN observations and the McClear-v3 estimates of B at Payerne and Xianghe. A good fit is

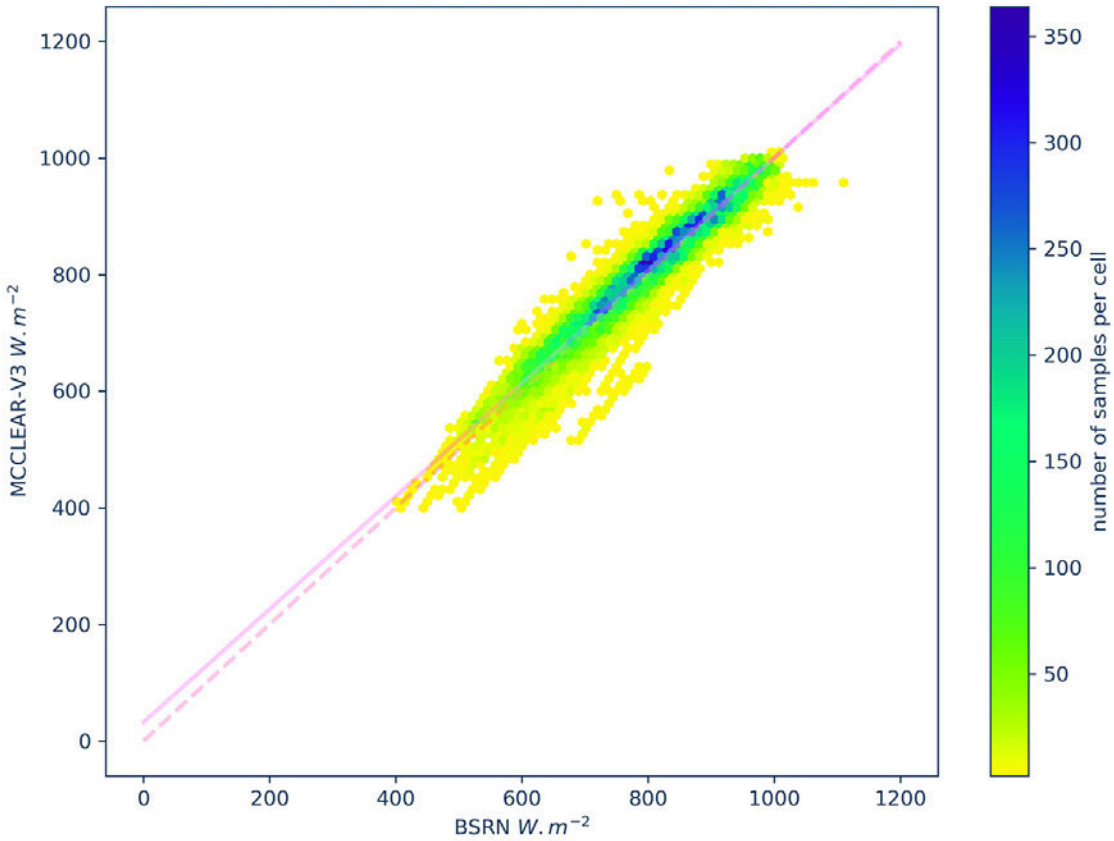

Figure 9: 2D histogram between BSRN observations (horizontal axis) and McClear-v3 estimates (vertical axis) for global irradiance at Xianghe. The color indicates the number of pairs in each class. The pink dotted line is the identity line, the full line results from a least-square fitting.

observed at Payerne: the points are fairly well aligned along the 1:1 line with a limited scattering. The graph at Xianghe exhibits more scattering and a pronounced underestimation of B. Lefèvre et al. (2013) reported that Xianghe is a rural city under the influence of the air pollution in Beijing and that the measurements of the co-located AERONET station showed that the fine mode was very often encountered. These particles may induce a strong contribution of the circumsolar area to the measurements of the beam by the pyrheliometer thus enhancing the underestimation by McClear-v3. An additional cause could be an overestimation of the actual τ_{550} by CAMS.

Table 7 reports the correlation coefficient at each site as well as the slope of the fitting line for B. The correlation coefficients for McClear-v3 are very large and greater than 0.98 at all sites, except Xianghe (0.90). They are marginally less than those observed for v2. The slopes are comprised between 0.94 and 1.04, except at Xianghe (0.83). They are marginally less than those for v2 but at several sites, they are closer to 1 than those for v2. The Ceamanos et al. (2014b) approach is not perfectly accurate this may explain the degradation observed in McClear-v3. This assumption may be replaced by using the direct model state of the CAMS model in future.

Table 7: Results for beam irradiance of the comparison of McClear-v3 versus BSRN side-by-side with those of the comparison of McClear-v2 versus BSRN. Correlation coefficient and slope of the line adjusted by least-squares fitting.

Station	Correl. coeff v2	Correl. coeff v3	Slope v2	Slope v3
Barrow	0.9808	0.9787	0.941	0.935
Palaiseau	0.9908	0.9898	0.997	0.987
Payerne	0.9888	0.9879	0.963	0.954
Carpentras	0.9918	0.9910	0.981	0.971
Xianghe	0.9107	0.9021	0.837	0.834
Tateno	0.9838	0.9825	1.027	1.010
Sede Boqer	0.9860	0.9847	0.958	0.953
Tamanrasset	0.9870	0.9866	1.036	1.011
Brasilia	0.9936	0.9933	1.050	1.037
Alice Springs	0.9956	0.9952	1.037	1.033
Lauder	0.9954	0.9950	0.954	0.948

Table 8 reports the bias and standard deviation and their values relative to the means of the measurements. The bias for McClear-v3 is negative (underestimation) at all sites, except at Brasilia. It ranges between −74 and 13 W m^{-2}, i.e. between −11 and 2 % of the means of the

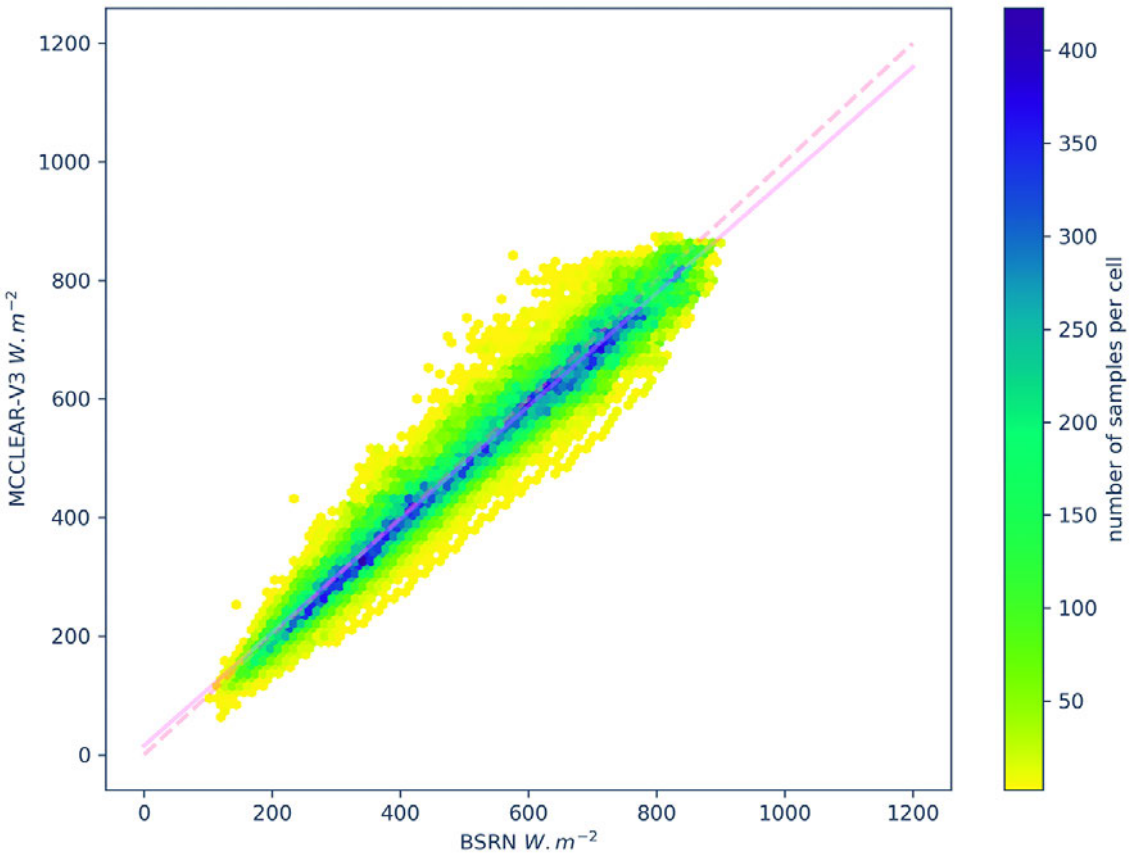

Figure 10: 2D histogram between BSRN observations (horizontal axis) and McClear-v3 estimates (vertical axis) for direct irradiance at Payerne. The color indicates the number of pairs in each class. The pink dotted line is the identity line, the full line results from a least-square fitting.

Table 8: Results for beam irradiance of the comparison of McClear-v3 versus BSRN side-by-side with those of the comparison of McClear-v2 versus BSRN. Bias and standard deviation and their values relative to the means of the measurements.

	Bias ($W\,m^{-2}$)		Standard deviation ($W\,m^{-2}$)		Relative bias (in %)		Relative standard deviation (in %)	
Station	v2	v3	v2	v3	v2	v3	v2	v3
Barrow	−26	−35	36	38	−6.3	−8.7	8.8	9.2
Palaiseau	−8	−20	36	37	−1.7	−4.1	7.3	7.6
Payerne	2	−9	39	41	0.3	−1.7	7.4	7.7
Carpentras	−4	−15	35	37	−0.8	−2.9	7.0	7.3
Xianghe	−28	−49	65	69	−4.3	−7.7	10.1	10.7
Tateno	−14	−26	41	41	−2.9	−5.4	8.4	8.6
Sede Boqer	−53	−74	40	42	−7.9	−11.0	6.0	6.2
Tamanrasset	17	−16	43	42	2.6	−2.4	6.5	6.4
Brasilia	27	13	34	34	4.8	2.3	6.1	6.0
Alice Springs	5	−5	32	34	0.8	−0.7	5.1	5.3
Lauder	−29	−36	33	35	−5.4	−6.6	6.1	6.4

observations. The greatest biases in absolute value are observed at Sede Boqer, then Xianghe, then Barrow and Lauder. The underestimation is more pronounced for v3 than for v2 (Table 8). The standard deviation is fairly constant and offers a limited range of variation between 34 and 42 $W\,m^{-2}$, except at Xianghe (69 $W\,m^{-2}$). Relative standard deviations range between 5.3 and 9.2 % (10.7 % at Xianghe). The standard deviation is slightly greater for v3 than for v2.

Similarly to G, the statistical quantities slightly vary from one year to another and with other variables: year, θ, τ_{550}, total contents in water vapor and ozone, and typical monthly Linke turbidity factors but no clear trend appears. The combination of a large correlation coefficient, the proximity to 1 of the slope and a small standard deviation of errors together demonstrate that McClear-v3 is capable of accurately capturing the variability of B at 1 min time-scale at most sites.

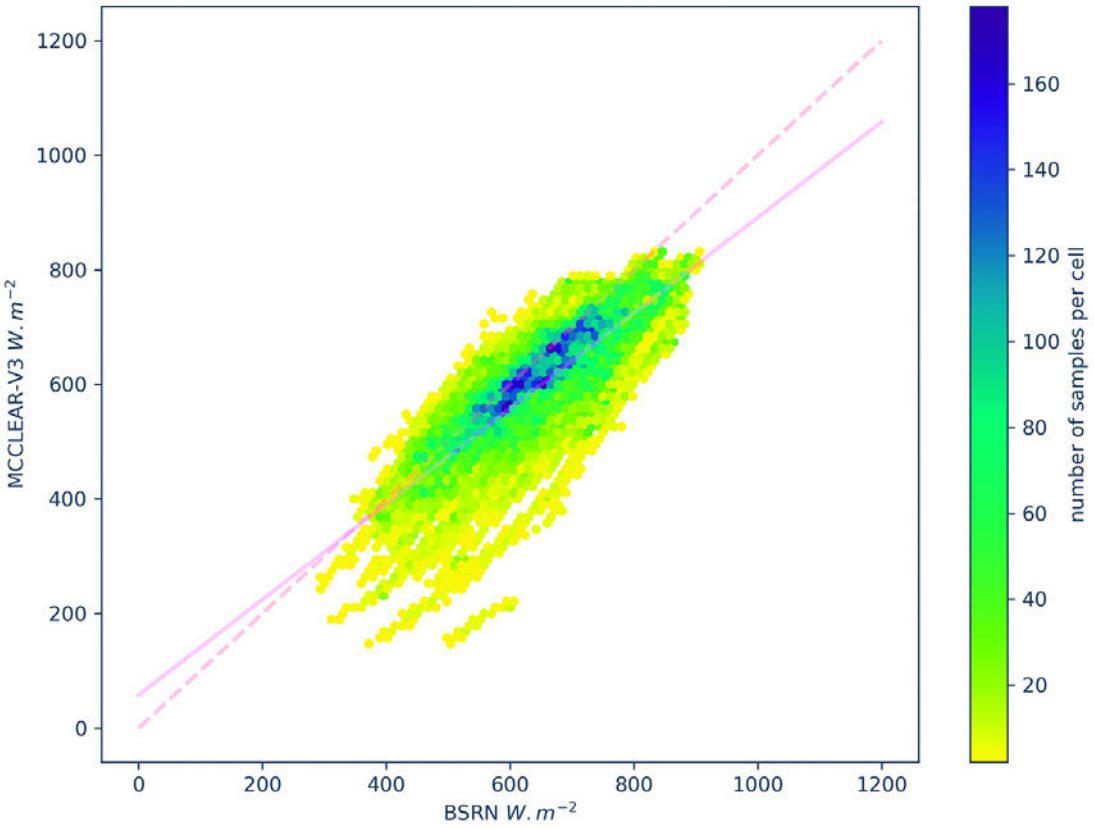

Figure 11: 2D histogram between BSRN observations (horizontal axis) and McClear-v3 estimates (vertical axis) for direct irradiance at Xianghe. The color indicates the number of pairs in each class. The pink dotted line is the identity line, the full line results from a least-square fitting.

6 Conclusions

The new clear-sky model McClear-v3 brings improvements by removing several artifacts of McClear-v2 such as the switch between aerosol classes or discontinuities in B and G with the solar zenithal angle. Furthermore, McClear-v3 offers potentials for future improvement that were not available in McClear-v2. Among the potential improvements are the future refinements of the modeling of the SOOT, INSO, WASO, DUST and SALT aerosol species in CAMS, and their vertical distribution as the current choice was very conservative. Other improvements on the computation of the diffuse SSI when the sun is below the horizon are made possible by adopting the computation of B and D instead of G and B, and by the removal of the MLB interpolation, which was calculable only when the sun is above the horizon.

The comparison between McClear-v3 estimates and measurements of 1 min means of global and direct SSI at eleven stations in the world shows that satisfactory results are attained for both G and B. These results are similar to those obtained with the version 2. Compared to the latter, McClear-v3 removes several artifacts and its estimates are continuous in space and time.

Assuming that the relative uncertainty of the measurements of G is 2 %, one may ask if the McClear-v3 estimates are compliant with "good quality", i.e. the relative uncertainty should not exceed 8 %. The total uncertainty takes into account the uncertainty of observations and the uncertainty of the estimates. It can be expressed in a first approximation as the quadratic sum of both uncertainties. As a consequence, the total relative uncertainty should not exceed 8 % (P95), or 4 % (P66) if the McClear-v3 estimates were of "good" quality. The relative standard deviations (P66) are all below 4 % and it can be concluded that to a first approximation, the quality of McClear-v3 estimates of G meets the WMO "good quality". This is not the case of B.

Similarly to v2, McClear-v3 is available as a model with all elements available on the same ftp site than v2 (ftp://ftp.oie-lab.net/pub/, last accessed: 2018-04-23). The combination of McClear-v3 with CAMS inputs is also available as a Web service. An interface has been developed to launch McClear-v3 within a standard Web browser and to obtain time series of global, diffuse and beam SSI under clear-sky at a given point and a given period for the following summarizations: 1 min, 15 min, 1 h, 1 day and 1 month. This interface can be launched via the catalog of products in the CAMS Web site (http://solar.atmosphere.copernicus.eu/, last access: 2018-04-25) or via the SoDa service (www.soda-pro.com, last access: 2018-05-02).

Acknowledgments

The research leading to these results has partly received funding from the Copernicus Atmosphere Monitoring Service, a program being operated by the European Centre for Medium-Range Weather Forecasts (ECMWF) on behalf of the European Union. The authors thank all operators of the ground stations of the BSRN network for their valuable measurements and the Alfred-Wegener Institute for hosting the BSRN website. The authors thank the team developing libRadtran (http://www.libradtran.org, last access: 2018-04-19). They thank X. Ceamanos, C. Emde and B. Mayer for their help about the modeling of the aerosols. They thank L. Saboret and E. Wey for their valuable help in setting up the McClear-v3 application on the Web. They also thank W. Wandji Nyamsi, Y. Aoun, S. Alfaro, Z. Qu, and Y. Eissa for their valuable contributions to the McClear model, their feedbacks, and their analysis.

References

Blanc, P., L. Wald, 2012: The SG2 algorithm for a fast and accurate computation of the position of the Sun. – Solar Energy **86**, 3072–3083, DOI:10.1016/j.solener.2012.07.018.

Blanc, P., B. Espinar, N. Geuder, C. Gueymard, R. Meyer, R. Pitz-Paal, B. Reinhardt, D. Renne, M. Sengupta, L. Wald, S. Wilbert, 2014a: Direct normal irradiance related definitions and applications: the circumsolar issue. – Solar Energy **110**, 561–577, DOI:10.1016/j.solener.2014.10.001.

Blanc, P., B. Gschwind, M. Lefèvre, L. Wald, 2014b: Twelve monthly maps of ground albedo parameters derived from MODIS data sets. – Proceedings of IGARSS 2014, held 13–18 July 2014, Quebec, Canada, USBKey, 3270–3272.

Cano, D., J.M. Monget, M. Albuisson, H. Guillard, N. Regas, L. Wald, 1986: A method for the determination of the global solar radiation from meteorological satellites data. – Solar Energy **37**, 31–39, DOI:10.1016/0038-092X(86)90104-0.

Ceamanos, X., D. Carrer, J.-L. Roujean, 2014a: Improved retrieval of direct and diffuse downwelling surface shortwave flux in cloudless atmosphere using dynamic estimates of aerosol content and type: application to the LSA-SAF project. – Atmos. Chem. Phys. **14**, 8209–8232, DOI:10.5194/acp-14-8209-2014, 2014.

Ceamanos, X., D. Carrer, J.-L. Roujean, 2014b: An efficient approach to estimate the transmittance and reflectance of a mixture of aerosol components. – Atmos. Res. **137**, 125–135, DOI:10.1016/j.atmosres.2013.09.009.

Cros, S., O. Liandrat, N. Sébastien, N. Schmutz, C. Voyant, 2013: Clear sky models assessment for an operational PV production forecasting solution. – 28th European Photovoltaic Solar Energy Conference and Exhibition, Sep 2013, France. pp.5BV.4.69, 2013.

Deneke, H.M., A.J. Feijt, R.A. Roebeling, 2008: Estimating surface solar irradiance from Meteosat SEVIRI-derived cloud properties. – Remote Sens. Env. **12**, 3131–3141, DOI:10.1016/j.rse.2008.03.012.

Dev, S., S. Manandhar, Y.H. Lee, S. Winkler, 2017: Study of clear sky models for Singapore. – Proc. Progress In Electromagnetics Research Symposium (PIERS).

Eissa, Y., S. Munawwar, A. Oumbe, P. Blanc, H. Ghedira, L. Wald, H. Bru, D. Goffe, 2015a: Validating surface downwelling solar irradiances estimated by the McClear model under cloud-free skies in the United Arab Emirates. – Solar Energy **114**, 17–31, DOI:10.1016/j.solener.2015.01.017.

Eissa, Y., M. Korany, Y. Aoun, M. Boraiy, M.A. Wahab, S. Alfaro, P. Blanc, M. El-Metwally, H. Ghedira, L. Wald, 2015b: Validation of the surface downwelling solar irradiance estimates of the HelioClim-3 database in Egypt. – Remote Sens. **7**, 9269–9291, DOI:10.3390/rs70709269.

Emde, C., R. Buras-Schnell, A. Kylling, B. Mayer, J. Gasteiger, U. Hamann, J. Kylling, B. Richter, C. Pause, T. Dowling, L. Bugliaro, 2016: The libRadtran software package for radiative transfer calculations (version 2.0.1). – Geosci. Model Dev. **9**, 1647–1672, DOI:10.5194/gmd-9-1647-2016.

Hess, M., P. Koepke, I. Schult, 1998: Optical properties of aerosols and clouds: The software package OPAC. – Bull. Amer. Meteor. Soc. **79**, 831–844, DOI:10.1175/1520-0477(1998)079<0831:OPOAAC>2.0.CO;2.

Ineichen, P., 2016: Validation of models that estimate the clear sky global and beam solar irradiance. – Solar Energy **132**, 332–344, DOI:10.1016/j.solener.2016.03.017.

Kopp, G., J.L. Lean, 2011. A new, lower value of total solar irradiance: evidence and climate significance. – Geophys. Res. Lett. **38**, L01706. DOI:10.1029/2010GL045777.

Lefèvre, M., L. Wald, 2016: Validation of the McClear clear-sky model in desert conditions with three stations in Israel. – Adv. Sci. Res. **13**, 21–26, DOI:10.5194/asr-13-21-2016.

Lefèvre, M., A. Oumbe, P. Blanc, B. Espinar, B. Gschwind, Z. Qu, L. Wald, M. Schroedter-Homscheidt, C. Hoyer-Klick, A. Arola, A. Benedetti, J.W. Kaiser, J.-J. Morcrette, 2013: McClear: a new model estimating downwelling solar radiation at ground level in clear-sky conditions. – Atmos. Meas. Tech. **6**, 2403–2418, DOI:10.5194/amt-6-2403-2013.

Mayer, B., A. Kylling, 2005: Technical note: The libRadtran software package for radiative transfer calculations – description and examples of use. – Atmos. Meas. Tech. **5**, 1855–1877, DOI:10.5194/acp-5-1855-2005.

Meftah, M., S. Dewitte, A. Irbah, A. Chevalier, C. Conscience, D. Crommelinck, E. Janssen, S. Mekaoui S., 2014: SOVAP/Picard, a spaceborne radiometer to measure the total solar irradiance. – Sol. Phys. **289**, 1885–1899, DOI:10.1007/s11207-013-0443-0.

Morcrette, J.-J., O. Boucher, L. Jones, D. Salmond, P. Bechtold, A. Beljaars, A. Benedetti, A. Bonet, J.W. Kaiser, M. Razinger, M. Schulz, S. Serrar, A.J. Simmons, M. Sofiev, M. Suttie, A.M. Tompkins, A. Untch, 2009: Aerosol analysis and forecast in the European Centre for Medium-Range Weather Forecasts Integrated Forecast System: Forward modeling. – J. Geophys. Res. **114**, D06206, DOI:10.1029/2008JD011235.

Mueller, R., K.F. Dagestad, P. Ineichen, M. Schroedter, S. Cros, D. Dumortier, R. Kuhlemann, J.A. Olseth, G. Piernavieja, C. Reise, L. Wald, L., D. Heinnemann, 2004: Rethinking satellite based solar irradiance modelling – The SOLIS clear sky module. – Remote Sens. Env. **91**, 160–174, DOI:10.1016/j.rse.2004.02.009.

Mueller, R., C. Matsoukas, A. Gratzki, H. Behr, R. Hollmann, 2009: The CM-SAF operational scheme for the satellite based retrieval of solar surface irradiance – a LUT based eigenvector hybrid approach. – Remote Sens. Env. **113**, 1012–1024, DOI:10.1016/j.rse.2009.01.012.

Ohmura, A., H. Gilgen, H. Hegner, G. Mueller, M. Wild, E.G. Dutton, B. Forgan, C. Froelich, R. Philipona, A. Heimo, G. Koenig-Langlo, B. McArthur,

R. Pinker, C.H. Whitlock, K. Dehne, 1998: Baseline Surface Radiation Network (BSRN/WCRP): New precision radiometry for climate research. – Bull. Amer. Meteor. Soc. **79**, 2115–2136, DOI:10.1175/1520-0477(1998)079<2115:BSRNBW>2.0.CO;2.

Oumbe, A., Z. Qu, P. Blanc, M. Lefèvre, L. Wald, S. Cros, 2014: Decoupling the effects of clear atmosphere and clouds to simplify calculations of the broadband solar irradiance at ground level. – Geosci. Model Develop. **7**, 1661–1669, DOI:10.5194/gmd-7-1661-2014, 2014. Corrigendum 7, 2409–2409.

Peel, M.C., B.L. Finlayson, T.A. McMahon, 2007: Updated world map of the Köppen-Geiger climate classification. – Hydrol. Earth Syst. Sci. **11**, 1633–1644, DOI:10.5194/hess-11-1633-2007.

Posselt, R., R.W. Mueller, R. Stöckli, J. Trentmann, 2012: Remote sensing of solar surface radiation for climate monitoring - the CM-SAF retrieval in international comparison. – Remote Sens. Env. **118**, 186–198, DOI:10.1016/j.rse.2011.11.016.

Qu, Z., P. Blanc, M. Lefèvre, L. Wald, A. Oumbe, 2011: Study of the MLB parameterisation for change in surface solar irradiance with sun zenith angle in clear sky. – Adv. Sci. Res. **6**, 233-236, DOI:10.5194/asr-6-233-2011.

Qu, Z., A. Oumbe, P. Blanc, B. Espinar, G. Gesell, B. Gschwind, L. Klüser, M. Lefèvre, L. Saboret, M. Schroedter-Homscheidt, L. Wald, 2017: Fast radiative transfer parameterisation for assessing the surface solar irradiance: The Heliosat-4 method. – Meteorol. Z. **26**, 33–57, DOI:10.1127/metz/2016/0781.

Raschke, E., A. Gratzki, M. Rieland, 1987: Estimates of global radiation at the ground from the reduced data sets of the International Satellite Cloud Climatology Project. – J. Climate **7**, 205-213, DOI:10.1002/joc.3370070302.

Remund, J., L. Wald, M. Lefèvre, T. Ranchin, J. Page, 2003: Worldwide Linke turbidity information. – Proceedings of ISES Solar World Congress, 16–19 June 2003, Göteborg, Sweden. CD-ROM published by International Solar Energy Society.

Rigollier, C., M. Lefèvre, L. Wald, 2004: The method Heliosat-2 for deriving shortwave solar radiation from satellite images. – Solar Energy **77**, 159–169, DOI:10.1016/j.solener.2004.04.017.

Schaaf, C.B., F. Gao, A.H. Strahler, W. Lucht, X.W. Li, T. Tsang, N.C. Strugnell, X.Y. Zhang, Y.F. Jin, J.P. Muller, P. Lewis, M. Barnsley, P. Hobson, M. Disney, G. Roberts, M. Dunderdale, C. Doll, R.P. d'Entremont, B.X. Hu, S.L. Liang, J.L. Privette, D. Roy, 2002: First operational BRDF, albedo nadir reflectance products from MODIS. – Remote Sens. Env. **83**, 135–148, DOI:10.1016/S0034-4257(02)00091-3.

Schroedter-Homscheidt, M., 2018: The Copernicus Atmosphere Monitoring Service (CAMS) Radiation Service in a nutshell, version 8. – Available at www.soda-pro.com/documents/10157/326238/Copernicus_radiation_service_in_nutshell_v8.pdf/8d11cb68-de4a-4c63-b260-9d68a98a5a27, last access: 2018-04-20.

Vuilleumier, L., M. Hauser, C. Félix, F. Vignola, P. Blanc, A. Kazantzidis, B. Calpini, 2014: Accuracy of ground surface broadband shortwave radiation monitoring. – J. Geophys. Res. Atmos. **119**, 13,838–13,860, DOI:10.1002/2014JD022335.

WMO, 2012: Guide to meteorological instruments and methods of observation. – WMO-No **8**, 2008 edition updated in 2010, World Meteorological Organization, Geneva, Switzerland.

International Astronomical Union General Assembly, 2015: Resolution B3 on recommended nominal conversion constants for selected solar and planetary properties. – Available at https://www.iau.org/static/resolutions/IAU2015_English.pdf, last accessed on 2017-05-07.

Zhong, X., J. Kleissl, 2015: Clear sky irradiances using REST2 and MODIS. – Solar Energy **116**, 144–164, DOI:10.1016/j.solener.2015.03.046.